Optimal Sensor Placement Design for High-Fidelity Deformation Measurement of Spaceborne Antenna

Yongxi He*, Songsheng Wang, Ye Liang and Xuechao Duan*

State Key Laboratory of Electromechanical Coupling, Xidian University, Xi'an 710071, China

Abstract: Spaceborne antennas are critical for high-precision communication between satellites and spacecraft. Their in-orbit reflective surfaces are susceptible to deformation under thermal loads and radiation exposure, leading to degraded electrical performance. Conventional deformation monitoring methods are limited by environmental sensitivity and system complexity, making accurate surface reconstruction challenging. This study presents a method for measuring and reconstructing antenna reflective surfaces using fiber Bragg grating (FBG) shape sensing technology. A structural model of the peripheral truss-cable net antenna is developed, and the Frenet-Serret curvature reconstruction algorithm is applied to recover surface geometry. An optimization model is further introduced to determine the optimal spatial distribution of sensors for a given number. The reconstructed surface based on the optimized layout is compared with the theoretical ideal surface. Results show that under optimized placement, reconstruction error decreases from 0.03 m to 0.01 m as sensor count increases from 3 to 15, eventually stabilizing. Marginal improvement analysis indicates that accuracy gains diminish beyond 10 sensors, suggesting a saturation effect. These results confirm the effectiveness of the proposed approach and provide a robust theoretical basis and practical guidance for sensor deployment in on-orbit monitoring of spaceborne antenna deformation.

Keywords: Cable-net antenna, Antenna shape measurement, Deformation reconstruction, Layout optimization, Shape sensor.

1. INTRODUCTION

Spaceborne antennas, as communication devices installed on satellites and spacecraft, undertake the crucial task of bidirectional information transmission between spacecraft and the ground, and are a key link for satellites to communicate with the outside world. During the in-orbit operation of communication satellites, due to the influence of factors such as temperature, solar radiation and microgravity, their reflector surfaces are prone to deformation, which leads to structural deformation and performance degradation [1, 2]. Therefore, conducting in-orbit deformation monitoring of deployable reflector surfaces is of significant importance.

The existing deformation measurement techniques mainly fall into three categories: three-dimensional laser scanning, stereo vision measurement, and fiber optic sensing monitoring. Three-dimensional laser scanning acquires the shape of the reflective surface through laser ranging and offers high measurement accuracy. However, its effectiveness is constrained by surface occlusion and structural complexity, and it is limited to application on flat surface structures [3]. Stereo vision measurement methods utilize multi-angle images for three-dimensional reconstruction and feature flexible system configurations. However, the measurement accuracy of the cameras depends on the observation baseline, camera focal length, and lighting conditions, making it challenging to maintain stable operation over extended periods in spatial environments with non-uniform illumination [4, 5]. This results in obvious limitations of the above methods in deformation monitoring within complex spatial environments and on large flexible reflective surfaces. In contrast, the optical fiber sensing monitoring method offers advantages such as high sensitivity, lightweight construction, and immunity to electromagnetic interference [6-8], making it well-suited for monitoring spatial structures. However, most existing studies on antenna shape monitoring based on optical fiber sensing employ empirical or uniform layout strategies, lacking optimized placement designs that account for the structural characteristics and deformation patterns of the antenna [9-11].

In response to these issues, this paper proposes a deformation monitoring and reconstruction method based on fiber Bragg grating (FBG) shape sensors. By establishing the geometric model of the antenna and optimizing the sensor layout, the surface reconstruction accuracy of the antenna is improved. According to the deformation characteristics of the antenna and the structural features of the peripheral truss-type deployable antenna, the geometric model of the antenna network truss structure is established using MATLAB software. FBG shape sensors are deployed on the upper cable grid surface of the model, and the antenna surface is reconstructed through the collection of surface deformation data.

*Address correspondence to this author at School of Mechano-Electronic Engineering, Xidian University, Xi'an, 710071, China;
E-mail: heyongxi@xidian.edu.cn, xchduan@xidian.edu.cn

E-ISSN: 3110-9780/25

The remainder of this paper is organized as follows: Section 2 introduces the modeling method of the cable-net and peripheral truss structure of the deployable antenna. Section 3 presents the deformation sensing principle based on FBG sensors and the Frenet-Serret curvature reconstruction method. Section 4 establishes the sensor layout optimization model and analyzes the influence of sensor number and placement on the accuracy of antenna surface reconstruction.

2. CONSTRUCTION OF THE ANTENNA CABLE–TRUSS STRUCTURAL MODEL

2.1. Design of Peripherally Supported Truss Structure

The peripheral supporting truss adopts a regular dodecagonal (12-sided) configuration, with all vertices located on a circle with a diameter of 10 m [12, 13]. During the modeling process, the supporting structure of the antenna is regarded as an assembly of multiple bar elements. To ensure that the structure is deployable, it is designed based on a Z-fold (zigzag) deployable mechanism. The truss consists of several identical parallelogram units; each unit includes two horizontal bars, two vertical bars, and a set of diagonal bars aligned along the diagonals of the parallelogram, forming a closed ring structure, as shown in Figure **1**.

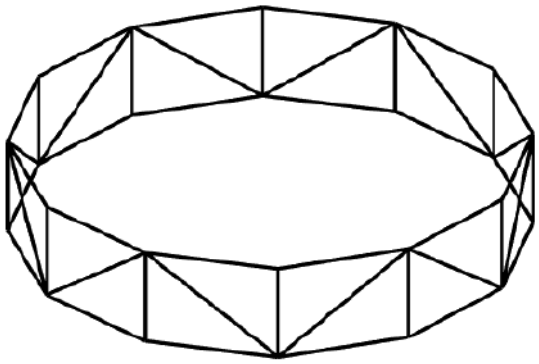

Figure 1: Dodecagonal peripheral supporting truss.

The length of each peripheral truss side is determined based on the aperture diameter of the antenna's parabolic reflector. Assuming the antenna aperture diameter is D and the total number of peripheral truss segments is *n*, the length of each horizontal truss member is calculated as:

$$l = \frac{D^2}{2}\left(1-\cos\frac{360}{n}\right) \tag{1}$$

where L is the length of the horizontal bar of the peripheral truss.

Subsequently, the heights of the upper and lower cable nets, as well as the distance between their corresponding vertices, are determined according to geometric relationships. Let h_1 denote the height of the upper cable net, h_2 the height of the lower cable net, and Δh the distance between the vertices of the two cable nets; then, the height of the peripheral truss is $h = h_1 + h_2 + \Delta h$. The length of the diagonal member, $L = \sqrt{\left(x_2 - x_1\right)^2 + \left(y_2 - y_1\right)^2 + \left(z_2 - z_1\right)^2}$, can be calculated using the Euclidean distance formula.

2.2. Cable Net Structural Configuration Design

In the modeling process, the antenna cable net is represented as a set of nodes interconnected by cable elements [14]. The nodes on the upper and lower cable nets are first numbered, and then sequentially connected from the inner to the outer layers in a point-to-point manner, forming a triangulated mesh. The positions of the upper cable net nodes are iteratively adjusted to achieve precise conformity with the ideal paraboloid, resulting in a "back-to-back" cable net structure (see Figure **2**). The upper cable net is constructed according to the parabolic equation, whereas the lower net, constrained solely by the antenna height, does not require high accuracy. The upper and lower nets are linked by vertical cables for stability, and the cable net structure is connected to the ring truss, with vertical cable lengths adjusted to control the upper net surface [15-17]. Recent studies have further refined the form-finding of cable nets by adopting modified force density approaches, enhancing both accuracy and efficiency [18].

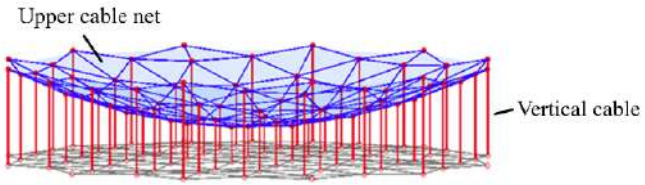

Figure 2: "Back-to-back" cable net structural configuration.

2.3. Assembly of the Integrated Cable Net–Truss Structural Model

The main structure of a deployable antenna reflector with a peripheral truss is formed by expanding outward from a central hexagon. Typically, when the number of peripheral truss sides n_s equals the number of supporting net sides, each of the six reflector surface vertices is directly connected to the corresponding vertex on the truss [19]. However, when the numbers differ, the connection strategy must be reconsidered.

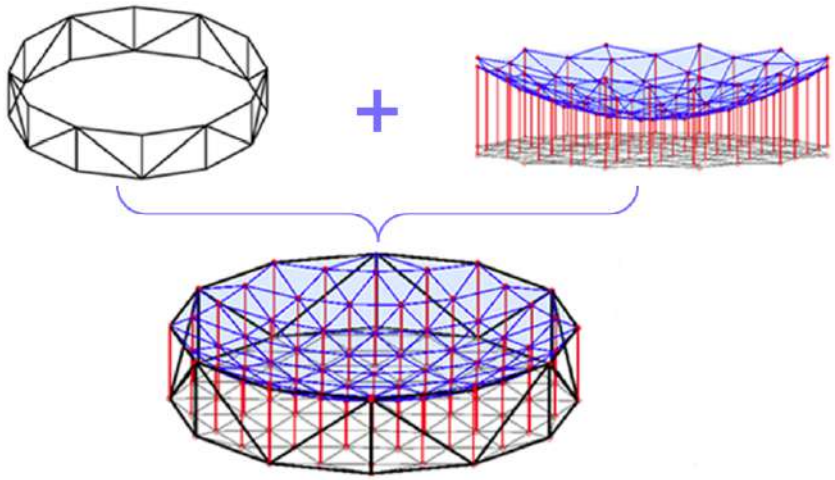

Figure 3: Complete model of the antenna cable net–truss structure.

Let n_1 and n_2 denote the total number of outer-edge nodes on the reflector surface and the peripheral truss, respectively.

$$n_1 = n_0 + 1 \tag{2}$$

$$n_2 = \frac{n_s}{6} + 1 \tag{3}$$

where n_0 denotes the number of segments of the main cable.

When assembling the antenna cable net–truss structure, the outer nodes $(0,1,2,\cdots,n_1)$ are matched to truss nodes $(0,a,b,\cdots,n_2)$, ensuring node 0 connects to node 0 and node n_1 to node n_2. This forms the complete net–truss structure shown in Figure **3**.

3. FBG-BASED ANTENNA SURFACE MEASUREMENT AND RECONSTRUCTION

3.1. Overview of the Measurement Principle of FBG Sensors

The operating principle of FBG is based on the periodic variation of the refractive index within the optical fiber. When light enters the fiber at a certain angle, only the light that satisfies the Bragg condition is reflected, while other wavelengths continue to propagate forward through the grating [20, 21]. According to the grating theory [22], each FBG reflects only a specific wavelength, and the reflected wavelength satisfies the Bragg condition:

$$\lambda_B = 2n_{eff}\Lambda \tag{4}$$

where λ_B is the central wavelength of the FBG, n_{eff} is the effective refractive index of the fiber core, and Λ is the grating period.

It can be seen from the above equation that the central wavelength of the FBG depends on the refractive index of the fiber core and the grating period [23, 24, 25]. When the FBG is subjected to external strain or changes in ambient temperature, both the refractive index and the grating period of the fiber will change, resulting in a shift of the central wavelength [26]. A schematic diagram of FBG shape sensor deformation is shown in Figure **4**.

Let the length of the FBG shape sensor be L, the distance from the FBG measurement point to the central axis be d, the radius of curvature be r, and the

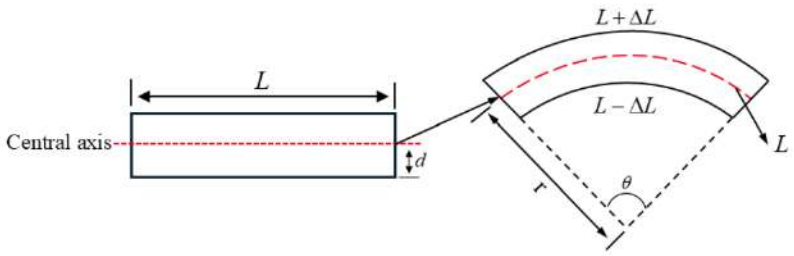

Figure 4: Schematic diagram of FBG shape sensor deformation.

central angle of the corresponding arc during bending be θ. The strain is denoted as $\varepsilon = \Delta L / L = kd$, where *k* is the bending curvature. The relationship between the shift in central wavelength and the strain is given by:

$$\Delta\lambda = \left(1 - P_e\right)\lambda_B \varepsilon \tag{5}$$

where P_e is the photo-elastic coefficient. Furthermore, the expression for curvature can be derived as follows:

$$k = \frac{\Delta\lambda}{\lambda_B d\left(1 - P_e\right)} \tag{6}$$

When the object bends, an axial strain ε is generated on its surface, which is related to the radius of curvature r as follows:

$$\varepsilon = \frac{d}{r} \tag{7}$$

By measuring the strain at each FBG, the local curvature can be obtained. Based on the obtained curvature, the Frenet curvature reconstruction algorithm is used to reconstruct the curve or surface of the object [27]. In addition, optical frequency domain reflectometry (OFDR) has been employed to reconstruct three-dimensional fiber shapes from strain data by utilizing the Frenet-Serret formulas, achieving millimeter-level accuracy in deformation monitoring [28]. The Frenet curvature reconstruction algorithm is a numerical method based on Frenet frame theory in differential geometry, enabling the recovery of continuous curvature information from discrete trajectory points [29, 30]. In this work, the Frenet–Serret differential equations are employed, and continuous curves are reconstructed from discrete curvature data through numerical integration, thereby reconstructing the antenna surface

3.2. Sensor Data Acquisition and Antenna Surface Reconstruction

Several representative curves are selected on the antenna cable net model to serve as simulated placement paths for the FBG sensors. The curvature and arc length information at each point on the cable net surface are extracted, and for ease of subsequent processing, the curves are sequentially numbered, as illustrated in Figure **5**.

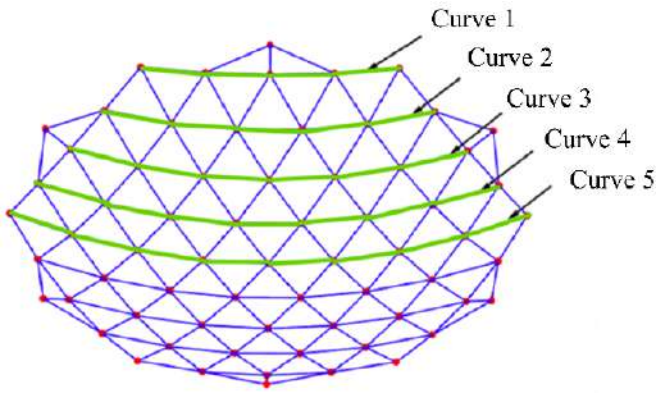

Figure 5: Numbering of curves on the antenna cable net surface.

Table 1: Curvature and Arc Length of each Point after Curve Interpolation (Partial)

Arc length on the negative x-axis	Curvature on the negative x-axis	Arc length on the positive x-axis	Curvature on the positive x-axis
0	0.10	0	0.10
0.02	0.09	0.02	0.09
0.04	0.09	0.04	0.09
0.06	0.09	0.06	0.09

Table 2: Reconstructed Data (Partial)

x	y_ reconstructed	y_ Theory	error	Arc length	Curvature
-2.49	1.29	1.30	-0.002	2.52	0.09
-2.48	1.29	1.30	-0.002	2.50	0.09
-2.46	1.28	1.29	-0.002	2.48	0.09
-2.42	1.28	1.28	-0.002	2.46	0.09
-2.40	1.27	1.27	-0.002	2.44	0.09

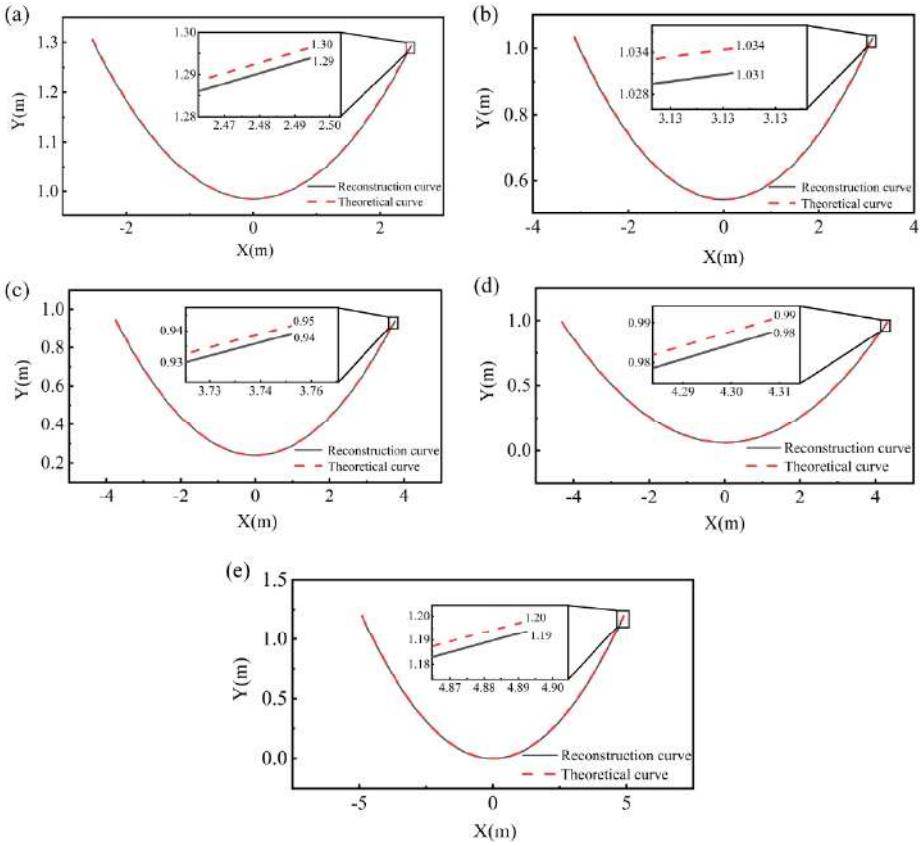

Figure 6: Comparison of the reconstructed results for five representative curves: (**a**) Curve 1, (**b**) Curve 2, (**c**) Curve 3, (**d**) Curve 4, and (**e**) Curve 5.

By fitting the parabolic surface of the upper cable net and interpolating the node coordinates, nine representative parabolic curves are obtained. Their curvature and arc length are then calculated for reconstruction, and the reconstructed curves are compared with the originals to evaluate the error.

Taking Curve 5 in Figure **5** as an example, its parabolic equation is $y = x^2 / 20$. Interpolation is performed on this curve at intervals of 0.02m, and the curvature and arc length of each interpolated point are obtained, as shown in Table **1**.

For each curve, interpolated data are used with the Frenet curvature algorithm to reconstruct curvature and arc length, as shown in Table **2**, with error analysis before and after reconstruction.

Using the above method, nine parabolic curves on the upper cable net surface of the antenna were reconstructed. Due to the symmetry of the paraboloid, only the first five curves are presented below.

Each reconstructed curve exhibits an error of approximately 0.01 m, indicating that the method can accurately reconstruct antenna surface curves. These curves are then fitted to reconstruct the surface, and the corresponding error analysis provides a basis for optimizing the sensor layout.

Based on the previously reconstructed curves, surface fitting is performed with a boundary condition constraint of $x^2 + y^2 = 25\left(z = 1.25m\right)$ to reduce edge errors. The resulting reconstructed antenna surface is shown in Figure **7**, with an error of 0.01 m compared to the original parabolic surface.

4. SENSOR LAYOUT OPTIMIZATION MODEL CONSTRUCTION AND ANALYSIS

4.1. Effect of Sensor Quantity and Placement on Surface Reconstruction

To investigate the influence of sensor quantity and arrangement position on the surface reconstruction accuracy of the antenna reflector, nine representative curves were selected on the upper cable net surface of the antenna for sensor layout configuration. By changing the number and distribution of sensors, the reconstruction results under each configuration are compared and analyzed with the theoretical surface to reveal the influence law of sensor layout on the

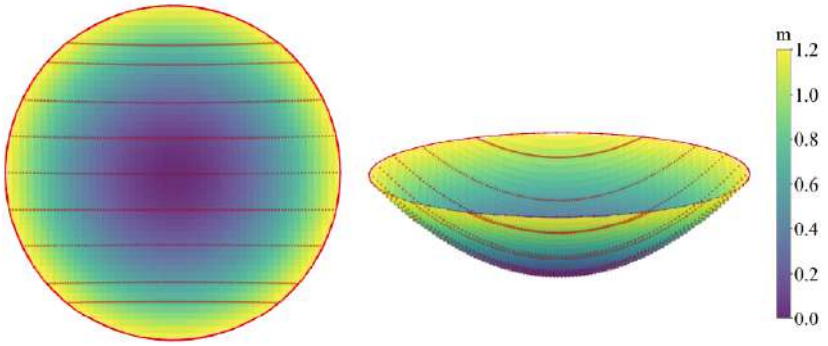

Figure 7: Reconstructed antenna surface before deformation.

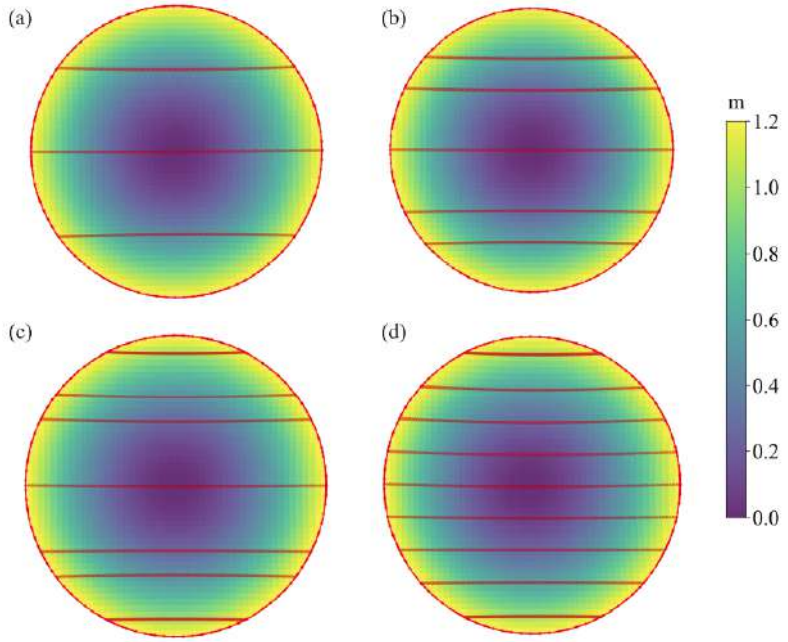

Figure 8: Comparison of surface fitting results with different numbers of sensors: (**a**) three, (**b**) five, (**c**) seven, and (**d**) nine.

reconstruction accuracy. To ensure surface smoothness and continuity, a cubic spline interpolation method is applied to the node coordinate data to generate the fitting curve, and the resulting curve is used as the FBG sensor layout path. The sensor arrangement is centered on the curve 5 passing through the vertex of the parabolic surface and symmetrically distributed on both sides to balance the positive and negative direction errors and improve the stability of the overall fitting. The optimal layout schemes under different sensor numbers were finally determined, providing a reference for the subsequent sensor layout optimization and high-precision surface reconstruction.

When the number of curves (sensors) is 3, the reconstruction error of the antenna surface is 0.03 m; for 5 sensors, the error is 0.015 m; for 7 sensors, 0.014 m; and for 9 sensors, 0.008 m. As the number of sensors increases, the reconstruction error decreases and gradually approaches a stable value, with sensor placement tending toward an optimal distribution. Based on this trend, an appropriate optimization algorithm is used to develop the sensor layout optimization model.

4.2. Construction of the Sensor Layout Optimization Model

Sensor placement directly influences surface reconstruction accuracy. Therefore, based on the previously identified placement patterns, a mathematical model for sensor layout optimization is formulated.

The theoretical surface to be reconstructed is defined by the following equation:

$$z = f(x,y) = \frac{x^2 + y^2}{20} \tag{8}$$

where $0 \le z \le 1.25m$.

Based on this, the sensor placement problem can be simplified to placement along the y-direction, subject to constraint $-R \le y_i \le R$. The maximum fitting error $E(\mathbf{y})$ is defined as:

$$E(\mathbf{y}) = \max \left| z_i^{fit} - z_i^{theory} \right| \tag{9}$$

The maximum fitting error $E(\mathbf{y})$ is obtained by interpolating the sensor (x,y,z)-data onto a two-dimensional grid and calculating the absolute difference between the reconstructed and theoretical surfaces, retaining only the maximum error within the surface. Here, $\left(z_i^{fit}\right)$ is the height of point i on the reconstructed surface, obtained by interpolation from the sensor data, and $\left(z_i^{theory}\right)$ is the height of point i on the theoretical paraboloid.

To avoid placement outside the measurement area and excessive proximity, boundary and spacing penalty functions, $P_b(\mathbf{y})$ and $P_s(\mathbf{y})$, are defined as follows:

$$P_b(\mathbf{y}) = \sum_{i=1}^{n} \begin{cases} 100 \times \left(|y_i| - R \right)^2, |y_i| > R \\ 0 \qquad\quad , |y_i| \le R \end{cases} \tag{10}$$

where 100 is the penalty factor, y_i is the y-coordinate of the i-th sensor, and $\left(|y_i| - R\right)$ is the boundary penalty term.

$$P_s(\mathbf{y}) = \sum_{i=1}^{n-1} \begin{cases} 100 \times \left(y_{i+1} - y_i - d_{\min} \right)^2, \left(y_{i+1} - y_i \right) < d_{\min} \\ 0 \qquad\qquad\qquad\quad , \left(y_{i+1} - y_i \right) \ge d_{\min} \end{cases} \tag{11}$$

where 100 is the penalty factor, y_{i+1} is the y-coordinate of the $(i+1)$th sensor, y_i is the y-coordinate of the i th sensor, and the minimum spacing $d_{\min} = 0.15m$ is set to ensure that the distance between adjacent sensors is not less than this value.

Combining the objective function and the penalty terms described above, the complete optimization objective function $J(\mathbf{y})$ is obtained:

$$J(\mathbf{y}) = E(\mathbf{y}) + P_b(\mathbf{y}) + P_s(\mathbf{y}) \tag{12}$$

To avoid local optima, initial sensor positions are generated using two strategies based on sensor quantity.

$$\begin{cases} y_i = 4.8 \cdot x_i \cdot \left(1 + 0.15 \cdot \left(x_i^3\right)\right), n \le 15 \\ y_i = base_i \cdot \left(1 - 0.1 \left(\dfrac{base_i}{4.5}\right)^2\right), n > 15 \end{cases} \tag{13}$$

Where $base_i = -4.5 + \dfrac{9}{n-1} \cdot (i-1)$. For fewer sensors, a cubic polynomial is used to achieve denser placement near the center and sparser at the edges. For a larger number of sensors, a quadratic adjustment is applied to ensure uniform distribution across the entire radius.

After generating the initial positions, the L-BFGS-B algorithm is employed for iterative optimization to obtain the global optimal solution of the objective function.

$$\mathbf{y}* = \arg\min_{y} J(\mathbf{y}) \tag{14}$$

where $\mathbf{y}*$ is the optimal solution and $J(\mathbf{y})$ is the value of the objective function.

4.3. Experimental Validation and Error Analysis

To validate the model, the optimal sensor positions are calculated for a given number of sensors. For n=4, the resulting y-values are 3.30 m, 1.09 m, -1.09 m, and -3.30 m, which are consistent with previous results. For n = 16, the model yields symmetric y-values of 4.18 m, 3.62 m, 3.06 m, 2.51 m, 1.95 m, 1.39 m, 0.84 m, and 0.28 m, further confirming its effectiveness.

Taking the case of four sensors as an example, their optimal layout positions on the antenna surface are shown in Figure **9**.

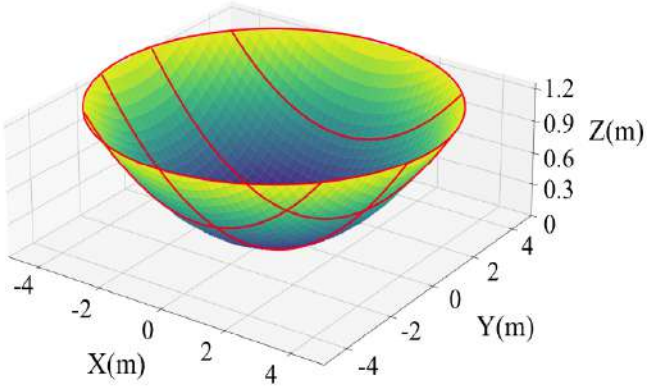

Figure 9: Optimized paraboloid reconstruction.

The reconstructed antenna surface is compared with the original theoretical surface, and the corresponding error distribution is presented below.

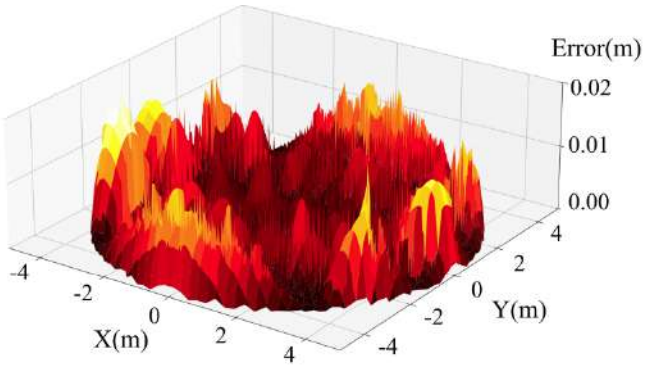

Figure 10: Reconstruction error distribution.

Comparison with the theoretical surface shows that the reconstruction error is about 0.02 m, with the maximum error at the surface edges due to fewer interpolation points at large y values. To analyze the relationship between sensor quantity and reconstruction accuracy, the model is run with varying sensor numbers, and the resulting errors are plotted, as shown below.

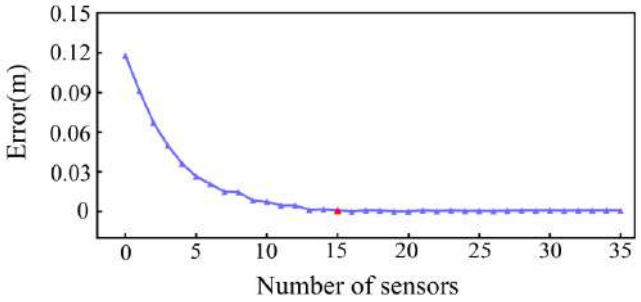

Figure 11: Error versus sensor quantity.

The results show that when the number of sensors is less than 15, the shape reconstruction error is large and exhibits significant fluctuations. When the number of sensors exceeds 15, the error is substantially reduced and tends to stabilize, with the maximum reconstruction error controllable at approximately 0.01 m. Compared with the structural occlusion issues inherent in traditional three-dimensional laser scanning and the high sensitivity of stereo vision methods to lighting conditions and baseline stability, the reconstruction method based on FBG curvature sensing with optimized sensor layout proposed in this paper demonstrates significant advantages. This method achieves a reconstruction accuracy of approximately 0.01 m under a limited sensor configuration and is not constrained by lighting conditions, enabling long-term stable deformation monitoring for large deployable spaceborne reflectors. This feature renders it suitable for critical applications such as in-orbit structural health assessment of spacecraft and real-time calibration of reflective surfaces, thereby providing a crucial guarantee for maintaining surface accuracy and communication performance of antenna systems. To further quantify the trade-off between sensor quantity and reconstruction accuracy, this paper introduces marginal improvement analysis to assess the contribution of additional sensors to error reduction. The results are presented in Figure **12**.

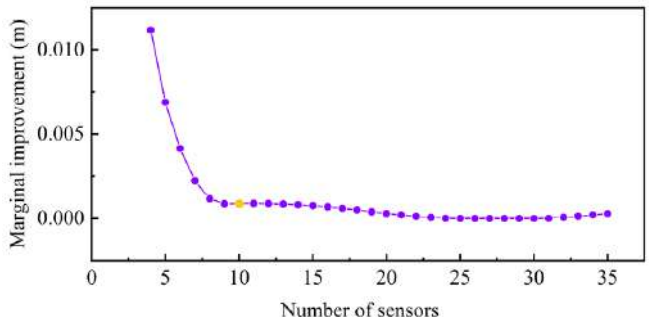

Figure 12: Error versus sensor quantity.

The results show that when the number of sensors is less than 10, the marginal improvement is significant, and adding sensors effectively enhances accuracy; however, when the number of sensors exceeds 10, the marginal improvement gradually approaches zero, indicating that while additional sensors may yield slight improvements, the associated cost increases substantially.

5. CONCLUSION

This paper investigates a deployable antenna with peripheral trusses by developing a geometric cable-net truss model. Virtual sensors are positioned on the upper surface to acquire deformation data, and the Frenet-Serret algorithm is employed to interpolate and reconstruct the antenna surface. Surface deformation is simulated through parameter adjustment, and the reconstruction results validate the effectiveness of the method. An optimization model is established to determine optimal sensor placement. With the optimized configuration, the reconstruction error stabilizes around 0.01 m, demonstrating a significant improvement in accuracy.

Conventional measurement methods such as 3D laser scanning and stereo vision can achieve millimeter-level precision only under ideal conditions.

Laser scanning is limited by occlusion, capturing only partial regions, while stereo vision is highly sensitive to lighting variations and baseline instability errors can reach the centimeter level under non-uniform illumination. In contrast, the proposed FBG-based approach enables real-time, in-situ, and remote monitoring. Using approximately 15 sensors, it achieves a reconstruction accuracy of about 0.01 m, offering an effective balance between measurement precision and deployment efficiency. Moreover, unlike uniform or empirically designed layouts, the proposed method dynamically adapts to varying sensor counts and structural characteristics, minimizing redundancy, reducing setup time, and lowering system complexity without compromising accuracy.

CREDIT AUTHORSHIP CONTRIBUTION STATEMENT

Yongxi He: Writing - original draft, Methodology, Conceptualization. **Songsheng Wang**: Software, Methodology, Data curation. **Ye Liang**: Visualization, Validation. **Xuechao Duan**: Supervision, Project administration.

DECLARATION OF COMPETING INTEREST

The authors declare that they have no known competing financial interests or personal relationships that could have appeared to influence the work reported in this paper.

ACKNOWLEDGEMENTS

This work was supported by the Natural Science Foundation of China (52305553), Natural Science Basic Research Project of Shaanxi Province (2025JC-YBMS-381).

REFERENCE

[1] Duan BY. Research status and development trend of large deployable space antennas. Chinese J. Electronic Mechanical Engineering 2017; 33(1): 1-14.

[2] He YX, Wang SS, Liang Y, Duan XC, Zhang YQ. Temperature-insensitive shape sensor for realtime deformation monitoring of discontinuous spaceborne antenna truss. Measurement 2026; 258: 119230. https://doi.org/10.1016/j.measurement.2025.119230

[3] Shang ZD, Chen JY, Zhou YL, Cong C, Zhao L, Meng XL, *et al*. Research on the rapid 3D measurement of satellite antenna reflectors using stereo tracking technique. Measurement 2024; 232: 114639. https://doi.org/10.1016/j.measurement.2024.114639

[4] Spencer Jr BF, Hoskere V, Narazaki Y. Advances in computer vision-based civil infrastructure inspection and monitoring. Engineering 2019; 5: 199-222. https://doi.org/10.1016/j.eng.2018.11.030

[5] Chen C, Zhang C, Ma J, He SZ, Chen J, Sun L, *et al*. FBG sensing data motivated dynamic feature assessment of the complicated CFRP antenna beam under various vibration modes. Buildings 2024; 14(7): 2249. https://doi.org/10.3390/buildings14072249

[6] Li XH, Niu ST, Bao H, Hu NG. Improved adaptive multi-objective particle swarm optimization of sensor layout for shape sensing with inverse finite element method. Sensors 2022; 22(14): 5203. https://doi.org/10.3390/s22145203

[7] Zhao J, Cheng YY, Zhang L, Li SG, Wang SX, Zhang FY, *et al*. Layout optimization of FBG sensor for aluminum alloy beam based on MOLA multiobjective optimization algorithm. IEEE Sensors Journal 2023; 23(13): 14129-14141. https://doi.org/10.1109/JSEN.2023.3276318

[8] Yu SQ, Hu D, Liu W. Vision-based optical 3D reconstruction technology and its application in crop information perception. Chinese J. Advances in Lasers and Optoelectronics 2024; 61(4): 49-57.

[9] Zhang ZH, Ye Q, Wang BY, Wang N, Meng GX. Untrained single scanning phase retrieval neural network for surface deformation measurement of large-aperture antennas. Optics and Lasers in Engineering 2024; 183: 108525. https://doi.org/10.1016/j.optlaseng.2024.108525

[10] Cui HH, Tian LF, Wang JR, Qu JX, Yang F, Guo JG. An efficient visual inspection planning method based on multi-objective optimization. Chinese J. Acta Optica Sinica 2024; 44(4): 215-226.

[11] Huang MA, Liu HL, Zhang QC, Wen JS, Liu QJ, Qing XL. Full-field dynamic strain reconstruction of rotating compressor blades based on FBG sensors. Smart Materials and Structures 2025; 34: 015001. https://doi.org/10.1088/1361-665X/ad95ce

[12] Gao CQ, Wang HL, Yang N, Guo JN, Liu F, Du JL. A large-span ring deployable perimeter truss for the mesh reflector deployable antenna. Symmetry 2025; 17(9): 1388. https://doi.org/10.3390/sym17091388

[13] Zhao J, Yang JG, Xiao Y, Ma XF. Deployment strategy and dynamic analysis of large ring truss antenna. International Journal of Aerospace Engineering 2022; 2022: 4725423. https://doi.org/10.1155/2022/4725423

[14] Tian DK, Shi ZW, Jin L, Yang XH, Liu RQ, Shi C. Pre-tension design and research of cable net structure for space modular deployable antenna. Advances in Engineering Software 2024; 195: 103685. https://doi.org/10.1016/j.advengsoft.2024.103685

[15] Tanaka H, Shimozono N, Natori M.C. A design method for cable network structures considering the flexibility of supporting structures. Transactions of the Japan Society for Aeronautical and Space Sciences 2008; 50(170): 267-273. https://doi.org/10.2322/tjsass.50.267

[16] Zhang SJ, Zhang SX , Gu YZ, Zhong W. Thermal design optimization method of mesh reflector antennas considering the interaction between cable net and flexible truss. Structural and Multidisciplinary Optimization 2023; 66: 68. https://doi.org/10.1007/s00158-023-03527-7

[17] Xue SD, Li XZ , Li XY, Dezhkam M. Automated design of cable-net structures with multi-objective state. Automation in Construction 2024; 160: 105288. https://doi.org/10.1016/j.autcon.2024.105288

[18] Li XY, Liu CB, Xue SD, Li XZ, Zhang C, Huang LY, *et al*. The modified force density method for form-finding of cable net structure. Thin-Walled Structures 2024; 195: 111363. https://doi.org/10.1016/j.tws.2023.111363

[19] Morterolle S, Maurin B, Quirant J, Dupuy C. Numerical form-finding of geotensoid tension truss for mesh reflector. Acta Astronautica 2012; 76: 154-163. https://doi.org/10.1016/j.actaastro.2012.02.025

[20] Zhao JC, Li YH, Song YM, An GW, Jia PG, Xiong JJ. Deformation reconstruction technology of satellite antenna based on FBG sensors. Chinese J. Infrared and Laser Engineering 2024; 53(6): 144-154.

[21] Li YH, Guan KS, Hu ZH, Chen YX. An optical fiber lateral displacement measurement method and experiments based on reflective grating panel. Sensors 2016; 16(6): 808. https://doi.org/10.3390/s16060808

[22] Amanzadeh M, Aminossadati SM, Kizil MS, Rakić AD. Recent developments in fiber optic shape sensing. Measurement 2018; 128: 119-173. https://doi.org/10.1016/j.measurement.2018.06.034

[23] Yuan LB. Characteristics of multi-core optical fibers and their sensing applications. Chinese J. Advances in Lasers and Optoelectronics 2019; 56(17): 171-195. https://doi.org/10.3788/LOP56.170612

[24] Yang M, Xu HW. Application of fiber Bragg grating sensing technology and physical model in bridge detection. Results in Physics 2023; 54: 107058. https://doi.org/10.1016/j.rinp.2023.107058

[25] Wang FW, Jiang Q, Ye MS, Zhang YX, Yu LH. Shape sensing technology based on fiber Bragg grating for flexible instrument. Measurement 2025; 243: 116282. https://doi.org/10.1016/j.measurement.2024.116282

[26] Choi S, Kim B, Lee H, Kim Y, Park H. A deformed shape monitoring model for building structures based on a 2D laser scanner. Sensors 2013; 13(5): 6746-6758. https://doi.org/10.3390/s130506746

[27] Milillo P, Porcu MC, Lundgren P, Soccodato F, Salzer J, Fielding E. The ongoing destabilization of the Mosul dam as observed by synthetic aperture radar interferometry. In Proc. 2017 IEEE International Geoscience and Remote Sensing Symposium (IGARSS) 2017; pp. 6279-6282. https://doi.org/10.1109/IGARSS.2017.8128442

[28] Xin W, Wang LJ, Liu Y, Zhang XD, Liu XJ. OFDR 3D shape reconstruction based on Frenet–Serret framework. Chinese J. Optical Instruments 2023; 45(2): 62-68.

[29] Kim HI, Kang LH, Han JH. Shape estimation with distributed fiber Bragg grating sensors for rotating structures. Smart Materials and Structures 2011; 20(3): 035011. https://doi.org/10.1088/0964-1726/20/3/035011

[30] Chen JT, Lee JW, Kao SK, Chou YT. Construction of a curve by using the state equation of Frenet formula. Journal of Mechanics 2021; 37: 454-465. https://doi.org/10.1093/jom/ufab014

Received on 05-10-2025 Accepted on 10-11-2025 Published on 24-11-2025

https://doi.org/10.66000/3110-9780.2025.01.03